Structural aspects and magnetic properties of Nd^{3+} doped nickel-zinc ferrites

K. Ratnaih[a], N. V. K. Prasad[a,*], M. C. Varma[b], G. S. V. R. K. Choudary[c]
[a]*Dept. of Physics, School of Sciences, GITAM (Deemed to be University), Bengaluru-India*
[b]*Dept. of Physics, Institute of Science, GITAM (Deemed to be University), Visakhapatnam-India*
[c]*Dept. of Physics and Electronics, Bhavan's Vivekananda College of SH &C, Secunderabad-India*

Magnetic properties and structural analysis of Nd(Neodymium) doped $Ni_{0.65}Zn_{0.35}Fe_2O_4$ using XRD, Rietveld Analysis, FTIR Spectroscopy and VSM are reported.Confirmation of secondary phase formation with increased Nd content is established. Cation distribution for neodymium substituted nickel-zinc ferritesis proposed by considering the deficiency of Fe^{3+} in $NiZnFe_2O_4$ due to secondary phase formation of $NdFeO_3$. The quality of present cation distribution was confirmed through close agreement of experimentally calculated lattice constant and Rietveld refinement. Changes in saturation magnetization with increased Nd content are explained on the basis of intensifying effect on energy exchange (inter-sublattice) between Ni–O–Nd and Ni–O–Fe concnerning Fe–O–Fe interaction, effect of replacing lower magnetic moment Nd^{3+} (3.62 μB) in place of Fe^{3+} (5 μB) and exchange developed between the cations existing at B-sites due to creation of oxygen vacancies.

(Received September 13, 2021; Accepted December 6, 2021)

Keywords: Ni-Zn ferrite, Neodymium, Rietveld analysis, Secondary phase, $NdFeO_3$

1. Introduction

Ferrite materials, among different oxide materials, carve their own space due to control that can be achieved on optical, electrical and magnetic properties. These properties make ferrite useful for many technological applications such as high-frequency core materials, microwave devices, microwave absorbers, multi-layer chip inductors [1,2]. They have been continuously attracting renewed attention with the advent of new applications like magnetic hyperthermia, MRI contrast agents, wastewater treatment, dye degradations and drug delivery even in the latest development detection of COVID-19 [3-11]. Ni-Zn ferrites are significant spinel ferrites due to their high electrical resistivity, moderate to high Curie temperature, dielectric constant and saturation magnetization of modrate values and sufficiently low losses belonging to $Fd\bar{3}m$ space. Thier charctrestics mainly depend on distribution of cations at tetrahedral (A) and octahedral (B) sites which can be determined by numerous factors such as stabilization energy, charge ordering, secondary phase formation, synthesis methods and temperature [12,13]. Superexchange interaction between cations at A,B sites control ferrites magnetic properties [14]. Doping of metal ions could change the cation occupancy, thus altering porosity, bond angles, bondlength, particle size [15] and superexchange interactions. Copper substitution in place of nickel improves densification [16], magnesium doping results in substantial changes in grain size, permeability, resistivity and loss factor [17]. Cobalt substitution was observed to lower coercivity [18], improve permeability [19] and frequency stability of permeability at higher frequencies. A drastic variation in distribution of cations has been reported for Cr substituted Ni-Co-Cu ferrite [20].

Rare-earth (RE) doping in ferrites produce secondary phase, increasing the lattice volume and lattice strain, altering the magnetic and electrical properties [21]. The change in these compounds' magnetic behaviour is governed by FeA–FeB interaction (3d electrons) and triggered by REB–FeB interaction originating from 3d–4f spin reoreintation [22]. The exchange interactions

* Corresponding author: drnvkprasad@gmail.com

between rare earth ions is mich weaker than that of RE^{3+}– Fe^{3+}ions as they are produced due to indirect interaction between 4f–5d to 5d–4f [23]. The role of RE ions in defining inter metallic compounds 3d–4f anisotropy is vigorous[24].

An increase in saturation magnetization and decrease in Curie temperature with substitution of Nd^{3+} in nickel ferrite was reported[25]. In another report, an increase in resistivity, decrease in lattice constant and dielectric loss with increased Nd^{3+} in zinc ferrite was observed[26]. Increase in photocatalytic activity and high solar activity in Nd^{3+} substituted nickel ferrite was reported[27]. Enhnaced dielectric constant and magneto capacitance of Ni ferrite on substituting Gd^{3+} and Nd^{3+} ions in place of Fe^{3+} ions in less amounts was observed[28]. They also reported appearance of net electric polarization which was attributed to the distortion caused by Gd^{3+} and Nd^{3+} ions having larger ionic radii compared to that of Fe^{3+} ions. Substitution of rare-earth ions like Y, Eu and Gd in Ni-Zn ferrites resulted in decreased relative loss factor and increased electrical resistivity [29]. Decrease in electrical resistivity and saturation magnetization for Gd deoped Ni–Zn ferrites was explained based on secondary orthoferrite phase $GdFeO_3$ formation[30].

The present work deals with the systematic study of the influence of Nd^{3+} substitution instead of Fe in $Ni_{0.65}Zn_{0.35}Fe_2O_4$. $Ni_{0.65}Zn_{0.35}Fe_2O_4$ [31,32] has been selected in this work because of high values of saturation magnetization , resistivity and magneto-dielectric performance at large frequencies [33] are reported for the same. Ferrite nanoparticles are synthesized by adopting techniques such as ball milling, co-precipitation, reverse micelles , hydrothermal , polymeric precursor, sol-gel and so on [34-39]. Agglomeration and particle coarsening have been reported when samples synthesized in most of these synthesis techniques are heated at higher temperatures. The reverse micelle is a better method to synthesize ferrite nanoparticles with narrow size distribution and insignificant agglomeration. In this work reverse micelle method is used to synthesize Nd doped Ni-Zn ferrite.

2. Experimental

To prepare $Ni_{0.65}Zn_{0.35}Nd_xFe_{2-x}O_4$ (x= 0.0, 0.02, 0.04, 0.06, 0.08 and 0.1) powders of nitrates Ni [$Ni(NO_3)_2.6H_2O$], Zn[$Zn(NO_3)_2.6H_2O$], Nd[$Nd(NO_3)_3$ $5H_2O$], Fe[Fe $(NO_3)_2.6H_2O$], Dodecyl sulphate sodium salt (SDS), n-Hexane(99%), 1-Butanol of analytical grade procured from HIMEDIAwere used without further purification.Metal nitrates in stoichiometric amounts are dissolved in deionized water separately and mixed for one hour using magnetic stirrer. These cationic solutions are used for further processing after improving homogeneity through stirring and mixing. Two micro-emulsion mixtures on combining water, SDS, 1butanol and n-hexane were prepared [40]. This solution on stirring for 1hour results in a transparent solution, which indicates the formation of a stable micelle.The precursor solution is dissolved in one of the microemulsion system and sonicated for 30 minutes. In other micro-emulsion, 5 Molar Sodium Hydroxide is added. These two were mixed and rapid magnetic stirring was done for an hour. Ferrite powder precipitated within the nanoreactor formed due to reverse micelle process was washed and dried 90°C for 8 hr.The powders were annealed for 1 hour at 500°C and then made into pellets using 20% PVA, applying a pressure of 10 psi and sintered at 1030 °C for 2 hours [32]. The powders obtained by grinding these pellets were subjected to further characterization.

3. Characterization

Shimadzu DTG-60 with a temperature range from RT to 1000 °C at a heating rate 10°C/min was used for thermogravimetric and differential thermal analysis (TGA & DTA) to provide information about thermal constancy and degradation pattern of constituents. Powder XRD measurements with Rigaku Make ULTIMA-IV model using Cu K_α radiation (1.5406 Å) between 10° to80° at 0.02^o per minute scan rate for all samples have been taken up. Using XRD data,

crystallite size was estimated using Scherrer's formula and Williamson-Hall (WH) plot using the following relations [41].

$$D = \frac{k\lambda}{\beta \cos\theta} \tag{1}$$

$$\beta \cos\theta = \left(\frac{k\lambda}{D}\right) + (4\varepsilon \sin\theta) \tag{2}$$

where 'θ' the Bragg's angle, 'D' the crystallite size, 'β' the FWHM ,'λ' the wavelength, 'k' ≈0.9 for spherical shaped grain), 4εsinθ is the strain effect on the crystallites.

The intercept of the plot between 4εsinθ (X-axis) and βcosθ (Y-axis) in Eq.3 that correspond to each diffraction peak provide mean crystallite size and slope gives the strain.

SEM was used to monitor morphology, grain size while Energy Dispersive X-Ray (EDX) analysis was used to assess chemical composition.

FTIR spectra of powders with different compositions was recorded between 4000 cm^{-1} to 400 cm^{-1} on Jasco FTIR-4200 of resolution +/- 0.5, wavenumber accuracy +/- 0.01 cm^{-1} and DLATGS Detector where in KBr is used as a solvent in 1:3 proportion. From the FTIR analysis, using band frequencies A- site (K_T) and B- site (K_o) force constants were calculated using the formula [41]

$$K = 4\pi^2 c^2 \nu^2 \mu \tag{3}$$

Room-temperature magnetic hysteresis was measured using a VSM (Moel 115 PAR-EG&G) on applying an external magnetic field of 20 kOe.

4. Results and Discussion

$Ni_{0.65}Zn_{0.35}Nd_xFe_{2-x}O_4$ (x= 0.0, 0.04, 0.08 and 0.1) powders were subject to thermogravimetric analysis (Fig. 1(a) -1(d)) at a heating rate of 10 °C/min to observe the phase transition during heat treatment.

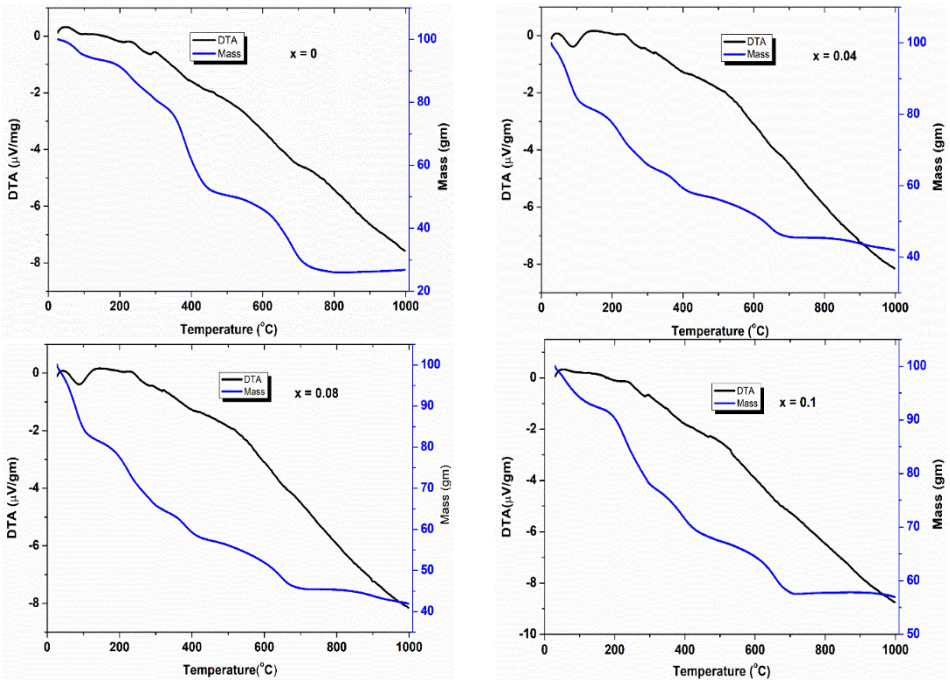

Fig. 1. DTA and TGA patterns of $Ni_{0.65}Nd_xZn_{0.35}Fe_{2-x}O_4$ (x = 0.0, 0.04, 0.08, 0.1).

The first weight loss of ~10% (16 % for x = 0.08) at temperature below 200°C and this is assigned to the dehydration process (Fig. 2).

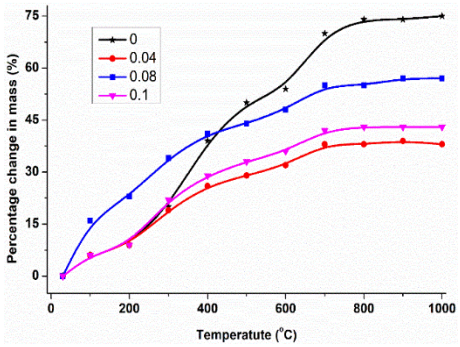

Fig. 2. Mass percentage vs Temperature for $Ni_{0.65}Nd_xZn_{0.35}Fe_{2-x}O_4$ (x = 0.0, 0.04, 0.08, 0.1)

The second weight loss observed between 200°C to 500°C is attributed to the breakdown of complexes, combustion of reactants and elimination of surfactants. Weight loss observed at temperatures 500-700 °C is due to the formation of spinel phase ferrite from corresponding metal oxides. Above 700 °C no significant weight loss was observed, indicating the completion of the crystallization process and the formation of nanocrystalline pure $Ni_{0.65}Zn_{0.35}Nd_xFe_{2-x}O_4$[42,43]. From TGA and DTA study, it is observed that the surfactants and other organic compounds are eliminated around 500 °C, and so, all the samples were annealed at temperature 500 °C.

Figure.3 shows high-resolution SEM images of $Ni_{0.65}Zn_{0.35}Nd_xFe_{2-x}O_4$ samples which display well-defined crystals of various shapes. EDX spectra of all samples (Fig. 3) confirms the presence of elements Ni, Zn, Nd, Fe, and O, indicating compositional uniformityand high purity of the samples.

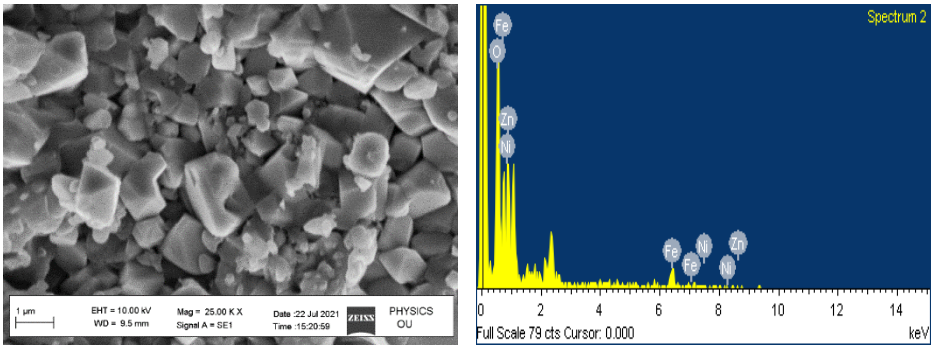

X= 0.00

X= 0.02

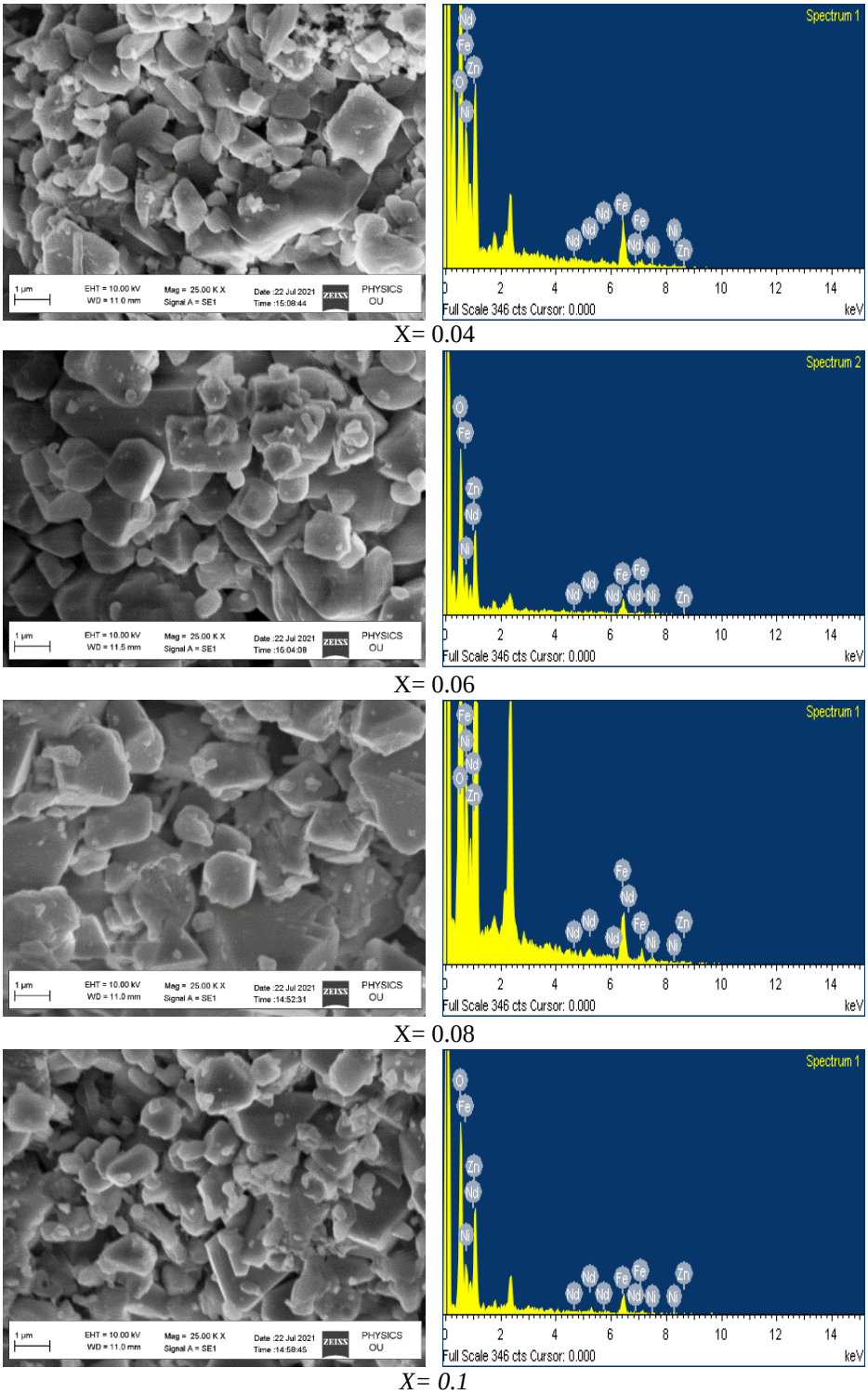

Fig. 3. SEM images and EDX spectra of $Ni_{0.65}Nd_xZn_{0.35}Fe_{2-x}O_4$

Figure 4 shows XRD patterns for all the $Ni_{0.65}Zn_{0.35}Nd_xFe_{2-x}O_4$ (x= 0.0, 0.02, 0.04, 0.06, 0.08 and 0.1) samples comprising of sharp lines corresponding to spinel structure, space group $Fd\bar{3}m$ and for x = 0.06, 0.08 and 0.1 samples an extra peak around 32^o indicates the presence of the orthoferrite phase.

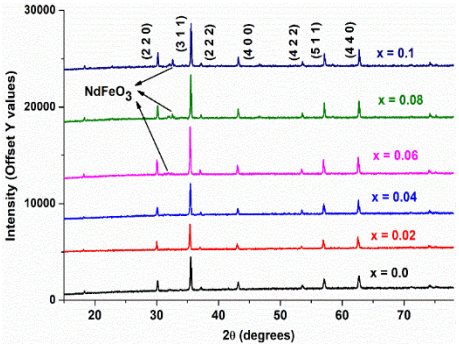

Fig. 4. XRD images of Nd doped Nickel-Zinc Ferrite samples

The XRD patterns of all the samples are in good agreement with spinel structure of nickel-zinc ferrite [18], and an extra peak at $2\theta=32.51^{o}$ is identified as $NdFeO_3$ with Crystallography open database card no.2003124 data. XRD patterns of all the samples were analyzed using Rietveld refinement as implemented inFullProfsuite [44] [Fig. 5]. The internal structure parameter of the oxygen (u), R-factors Rp, Rwp, χ^2 values and the goodness of fit are presented in Table 2.

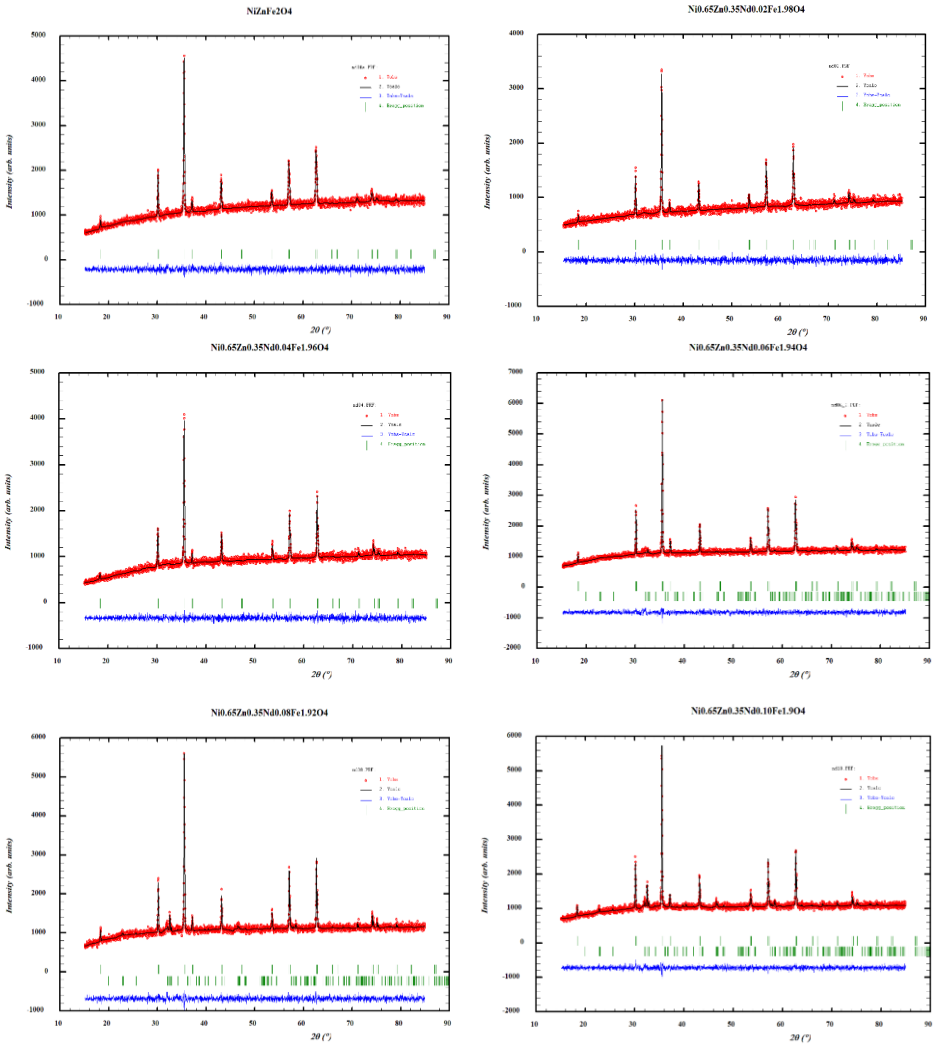

Fig. 5. Rietveld refinements patterns for $Ni_{0.65}Nd_xZn_{0.35}Fe_{2-x}O_4$ ferrites for x=0,0.02, 0.04, 0.06, 0.08, 0.10.

XRD analysis established the formation of the secondary phase of NdFeO3 from x = 0.06. This analysis also reveals that the peak intensity of $NdFeO_3$ phase increases with the increase of Nd concentration upto x = 0.1. Rietveld refinement also suggests an increase in volume concentration of $NdFeO_3$ as seen from table 1.The formation of $NdFeO_3$ should also lead to the deficiency of Fe^{3+} in $Ni_{0.65}Zn_{0.35}Fe_2O_4$structure, leading to the formation of Fe^{2+}, structure deformation, oxygen ion vacancies, and defects.

Table 1. Rp, Rwp, χ^2, GOF parameters and volume fraction obtained from Rietveld refinement for neodymium-doped Ni-Zn ferrites.

x	Lattice constant	u	Rp	Rwp	χ^2	GoF-index	Volume % of $Ni_{0.65}Zn_{0.35}Nd_xFe_{2-x}O_4$	Volume % of $NdFeO_3$
0	8.3766	0.256	3.05	3.86	1.77	1.3	100	0
0.02	8.3711	0.257	3.64	4.60	1.74	1.3	100	0
0.04	8.3728	0.253	3.50	4.40	1.79	1.3	100	0
0.06	8.3747	0.258	3.00	3.79	1.68	1.3	98.78	1.22
0.08	8.3753	0.259	3.29	4.14	1.92	1.4	94.23	5.77
0.1	8.3754	0.258	3.28	4.13	1.83	1.3	91.72	8.28

The calculation of lattice parameters has been made from each peak of the X-ray pattern using the equation $a = d\sqrt{h^2 + k^2 + l^2}$ and diffraction angle θ. Precise lattice parameter determination has been attained from the extrapolation of the calculated lattice parameter against Nelson-Riley function ($F(\theta) = \frac{1}{2}\left(\frac{\cos^2\theta}{\sin\theta} + \frac{\cos^2\theta}{\theta}\right)$) for which the function is zero.The lattice constant was also obtained from cation distribution, Rietveld refinement. The crystallite sizes are also calculated using the Scherrer method, Williamson-Hall method [41], and Rietveld refinement in table 3.

Table 3. Crystallite size and lattice constant for $Ni_{0.65}Zn_{0.35}Nd_xFe_{2-x}O_4$.

	Crytallite Size (nm)			Lattice constant (Å)		
x	Rietveld	Scherer	WH plot	Nel rel	Rietveld	Cation dist
0	87.3	65.2	20.7	8.372	8.376	8.375
0.02	112.8	77.1	24.7	8.374	8.371	8.371
0.04	112.5	77.8	16.8	8.3751	8.372	8.372
0.06	130.4	79.5	26.2	8.3748	8.373	8.373
0.08	135.2	77	19.8	8.3733	8.375	8.375
0.1	138.9	73.6	18.5	8.3713	8.3759	8.376

Some reports suggest that Nd atoms enter spinel structure of $NiZnFe_2O_4$ up to the percolation limit [45]. We assumed that $NdFeO_3$ formation begins from x =0.02, but could not be detected in XRD as this quantity is less than 1% for x =0.02, 0.04 evident from the volume% obtained in Rietveld analysis. From x =0.06 the $NdFeO_3$ is significant enough to be detected in XRD.Using this supposition from analysis of XRD and Rietveld refinement the net distribution of cations for Nd doped Ni-Zn ferrites is proposed as follows

$$(Zn_{0.35}\ Ni_{0.055}\ Fe_{0.595})[Ni_{0.595}\ Fe_{1.405}]O_4$$

$$(Zn_{0.35}\ Ni_{0.055}\ Fe_{0.595})[\ Ni_{0.595}Nd_{0.014}\ Fe_{1.379}]O_4$$

$$(Zn_{0.35}\ Ni_{0.055}\ Fe_{0.595})[\ Ni_{0.595}Nd_{0.0304}\ Fe_{1.3554}]O_4$$

$$(Zn_{0.35}\ Ni_{0.055}\ Fe_{0.595})[\ Ni_{0.595}Nd_{0.0468}\ Fe_{1.3318}]O_4$$

$$(Zn_{0.35}\ Ni_{0.055}\ Fe_{0.595})[\ Ni_{0.595}Nd_{0.0635}\ Fe_{1.3085}]O_4$$

$$(Zn_{0.35}\ Ni_{0.055}\ Fe_{0.595})[Ni_{0.595}Nd_{0.0798}\ Fe_{1.2848}]O_4$$

To confirm the exactness of proposed cation distribution, lattice constant for $Ni_{0.65}Zn_{0.35}Fe_2O_4$ was calculated from the equation [46]

$$a_{th} = \frac{8}{3\sqrt{3}}\left[(r_A + R_o) + \sqrt{3}(r_B + R_o)\right] \tag{26}$$

Here r_A and r_B reprsent radii of A,B sites, R_o the radius of oxygen ion (1.32 Å). The values r_A and r_B can be determined using the following formulae.

$$r_A = (0.0114\ r_{Ni^{2+}} + 0.35\ r_{Zn^{2+}} + 0.6386\ r_{Fe^{3+}}) \tag{27}$$

$$r_B = \frac{1}{2}(0.6386\ r_{Ni^{2+}} + 1.3614\ r_{Fe^{3+}}) \tag{28}$$

Shannon ionic radii of Ni^{2+}, Zn^{2+}, and Fe^{3+} ions at tetrahedral and octahedral coordinations have been considered for this calculation [47, 48]. The accuracy of suggested cation distribution has been confirmed by close agreement of lattice parameter obtained from experimental calculation, Rietveld refinement technique and proposed cation distribution as given in Table 2. FTIR spectra of $Ni_{0.65}Zn_{0.35}Nd_xFe_{2-x}O_4$ is shown in Figure 6. Enlarged view of peaks corresponding to both tetrahedral and octahedral site are also shown in the figure.

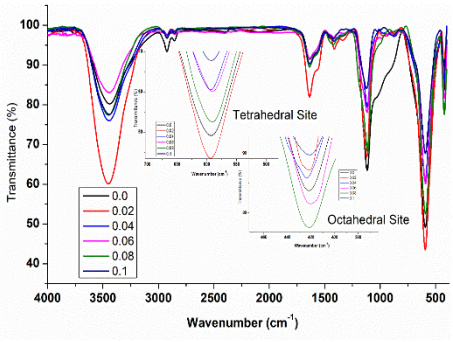

Fig. 6. FTIR absorption spectra of $Ni_{0.65}Nd_xZn_{0.35}Fe_{2-x}O_4$ ferrites.

Two significant absorption bands conforming to Fe-O bonds at A and B sites in the range of 400–600 cm^{-1} are assigned,which divulge the formation of spinel phase [49]. The higher wave number absorption band ν_1 with greater intensity associated with A site is in the range of 595–590 cm^{-1} and the lower wavenumber absorption band ν_2 comparitively lesser intensity is in the range of 420–424 cm^{-1}. Wavenumbers and force constants associated with both A and B sites are almost constant with Nd doping, as shown in Table 4. Thus, no significant conclusion can be drawn regarding cation ion redistribution with increasing Nd^{3+} content from these FTIR spectra.

Table 4.Wavenumbers and Force constants for $Ni_{0.65}Zn_{0.35}Nd_xFe_{2-x}O_4$.

x	ν_T cm^{-1}	ν_O cm^{-1}	F_T Nm^{-1}	F_O Nm^{-1}
0	593	421.4	257	130
0.02	594	421.4	258	130
0.04	593	423.3	257	131
0.06	591.1	420.4	256	129
0.08	591.1	421.4	256	130
0.1	593	421.4	257	130

Figure 7 displays the MH loops of current samples at room temperature. Saturation magnetization (Ms), remanent magnetization (Mr) and coercive force (Hc) values are presented in Table 5.

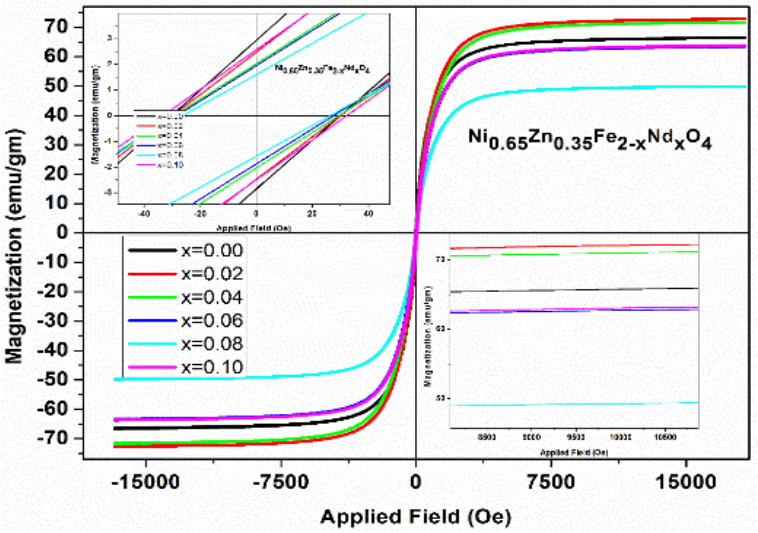

Fig. 7. Hysteresis loops of $Ni_{0.65}Nd_xZn_{0.35}Fe_{2-x}O_4$ ferrites

Table 5. Saturation Magnetization (Ms), Remanant Magnetization (Mr) and Coercive Force (Hc) for $Ni_{0.65}Zn_{0.35}Nd_xFe_{2-x}O_4$.

x	Ms	Hc	Mr	Mr/Ms
0	66.56	30.06	2.9	0.043
0.02	72.8	29.90	2.47	0.034
0.04	71.7	29.3	2.03	0.028
0.06	63.42	27.9	1.95	0.031
0.08	49.84	26.25	1.61	0.032
0.1	63.73	32.74	2.57	0.04

The saturation magnetization increases upto x = 0.02, then decreases with increase in Nd^{3+}concentration upto x = 0.08 and again increases for x= 0.1. For x = 0.02 value of Ms increased with increased exchange energy(inter-sublattice) between Ni–O–Nd and Ni–O–Fe [25]. But with a further increase in Nd^{3+}, saturation magnetization due to the dominating effect of replacing lower magnetic moment Nd^{3+} (3.62 μB) in place of Fe^{3+} (5 μB) results in an effective decrease in the magnetic moment [50,51]. Also net magnetic moment decreases due to formation of higher quantity antiferromagnetic $NdFeO_3$ phase at room temperature [52]. An increase in saturation magnetization for Nd concentration of 0.1 may be due toformation of oxygen ion

vacancies and defects. The experimentally observed increase in magnetization for x = 0.1 sample could be because of the ferromagnetic interaction developed between the cations existing at B-sites due to the creation of oxygen vacancies which in turn are affected by the amount of secondary orthoferrite $NdFeO_3$ phase. From Rietveld analysis, the decrease in iron content in spinel ferrite lattice has been established and the simultaneous formation of orthoferrite phase leads to oxygen vacancies. Thus, oxygen vacancies created will develop ferromagnetic interaction between Fe^{3+} ions at B-sites of spinel ferrite lattice, increasing the saturation magnetization [53]. This kind of observation is further strengthened by the study reported by S Ayyappan et al., [54], where they observed the creation of oxygen vacancies enhanced spin disorder leading to magnetic ordering. In a more recent study, Zihan Wang et al, [55] have explained how the oxygen vacancies break Fe^{3+}-O^{2-}-Fe^{3+} superexchange interactions and result in Fe^{3+}-Fe^{3+} ferromagnetism configuration.

5. Conclusions

Three regions of weight loss are observed between 0°Cto 200°C,200°C to 500°C, 500°C - 700 °C which are assigned to the dehydration of residual water, breakdown of complexes, combustion of reactants, elimination of surfactants and spinel phase ferrite from corresponding metal oxides respectively. Secondary phase formation of $NdFeO_3$ with increased Nd content is observed. Cation distribution for neodymium substituted nickel-zinc ferrites is proposed by considering deficiency of Fe^{3+} in $NiZnFe_2O_4$ due to secondary phase formation of $NdFeO_3$. The exactness of the proposed cation distribution has been confirmed by close agreement of lattice constant obtained from experimental calculation, Rietveld refinement technique and proposed cation distribution. Enhancing effect on inter-sublattice exchange energy between Ni–O–Nd and Ni–O–Fe concerning Fe–O–Fe interaction, effect of replacing lower magnetic moment Nd^{3+} (3.62 μB) in place of Fe^{3+} (5 μB), and interaction developed between the cations existing at B-sites due to creation of oxygen vacancies are found to the basis for the observed changes in saturation magnetization.

References

[1] A. M. Kumar, K. S. Rao, M. C. Varma, K. H. Rao, Journal of Magnetism and Magnetic Materials **471**, 262 (2019).

[2] S. Bharadwaj, T. Ramesh, S. R. Murthy, Journal of Electroceramics **31**(1-2), 81 (2013).

[3] M. A. Almessiere, Y. Slimani, A. D. Korkmaz, N. Taskhandi, M. Sertkol, A. Baykal, Sagar E. Shirsath, İ. Ercan, B. Ozçelik, Ultrasonics Sonochemistry **58**, 104621 (2019).

[4] Y. Slimani, M. A. Almessiere, S. Güner et al., J Sol-Gel Sci Technol **95**, 202 (2020).

[5] Y. Slimani, M. A. Almessiere, A. Demir Korkmaz, S. Guner, H. Güngüneş, M. Sertkol, A. Manikandan, A. Yildiz, S. Akhtar, Sagar E. Shirsath, A. Baykal, Ultrasonics Sonochemistry **59**, 104757 (2019).

[6] Y. Slimani, M. A. Almessiere, M. Sertkol, Sagar E. Shirsath, A. Baykal, M. Nawaz, S. Akhtar, B. Ozcelik, I. Ercan, Ultrasonics Sonochemistry **57**, 203 (2019).

[7] M. A. Almessiere, Y. Slimani, S. Guner, M. Sertkol, A. Demir Korkmaz, Sagar E. Shirsath, A. Baykal, Ultrasonics Sonochemistry **58**, 104654 (2019).

[8] M. A. Almessiere, Y. Slimani, S. Güner, A. Baykal, I. Ercan, Journal of Rare Earths **37**, 871 (2019).

[9] A. D. Korkmaz, S. Güner, Y. Slimani et al., Microstructural, J Supercond Nov Magn **32,** 1057 (2019).

[10] S. Akhtar, S. Rehman, M. A. Almessiere, F. A. Khan, Y. Slimani, A. Baykal, Nanomaterials **9**(11), 1635 (2019).

[11] S. B. Somvanshi, P. B. Kharat, T. S. Saraf, S. B. Somwanshi, S. B. Shejul, K. M. Jadhav, Mater. Res. Innovat 1, 6 (2020).

[12] J. Massoudi, M. Smari, K. Nouri, E. Dhahri, K. Khirouni, S. Bertaina, L. Bessais, RSC

Advances **10**(57), 34556 (2020).
[13] T. Dippong, E. A. Levei, L. Diamandescu, I. Bibicu, C. Leostean, G. Borodi, L. B. Tudoran, Journal of Magnetism and Magnetic Materials **394**, 111 (2015).
[14] N. Rezlescu, E. Rezlescu, C. Pasnicu, M. L. Craus, J. Phys.: Condens. Matter **6**, 5707 (1994).
[15] T. Dippong, O. Cadar, I. G. Deac, M. Lazar, G. Borodi, E. A. Levei, Journal of Alloys and Compounds **828**, 154409 (2020).
[16] G. S. V. R. K. Choudary, P. Prameela, M. Chaitanya Varma, A. Mahesh Kumar, K. H. Rao, Indian Journal of Materials Science **2013**, 350707 (2013).
[17] M. Chaitanya Varma, S. Bharadwaj, G. S. V. R. K. Choudary, K. S. R. Murthy, K. H. Rao, International Journal of Modern Physics B **31**(09), 1750063 (2017).
[18] J. N. P. K. Chintala, M. C. Varma, G. S. V. R. K. Choudary, K. H. Rao, J Supercond Nov Magn (2021).
[19] D. R. S. Gangaswamy, G. S. V. R. K. Choudary, M. C. Varma, S. Bharadwaj, K. H. Rao, Journal of Superconductivity and Novel Magnetism **31**(11), 3753 (2018).
[20] M. C. Varma, S. Bharadwaj, K. V. Babu, Physica B: Condensed Matter **556**, 175 (2019).
[21] S. E. Jacobo, S. D. Uhalde, H. R. Bertorello, J.Magn.Magn.Mater. **272**, 2253 (2004).
[22] S. Chikazumi, NewYork, Oxford University Press,1997.
[23] N. Rezlescu, E. Rezlescu, C. Pasnicu, M. L. Craus, J. Phys. Condens. Matter. **6**, 5707 (1994).
[24] Lijun Zhao, Hua Yang, (Materials and Manufacturing Processes **23**(1), 5 (2007).
[25] T. J. Shinde, A. B. Gadkari, P. N. Vasambekar, Journal of Alloys and Compounds **513**, 80 (2012).
[26] T. J. Shinde, A. B. Gadkari, P. N. Vasambekar, J. Magn. Magn. Mater. **322**, 2777 (2010).
[27] K. N. Harish, H. S. B. Naik, P. N. Prashanth Kumar, R. Viswanath, ACS SustainableChem. Eng. **1**, 1143 (2013).
[28] K. K. Bharathi, J. A. Chelvaneb, G. Markandeyulu, J. Magn. Magn. Mater. **321**, 3677 (2009).
[29] G. L. Sun, J. B. Li, J. J. Sun, X. Z. Yang, J. Magn. Magn. Mater. **281**, 173 (2004).
[30] A. Mahesh Kumar, M. Chaitanya Varma, G. Choudary, P. Prameela, K. H. Rao, Journal of Magnetism and Magnetic Materials **324**(1), 68 (2012).
[31] J. N. P. K. Chintala, S. D. Kaushik, M. C. Varma, G. S. V. R. K. Choudary, K. H. Rao, Journal of Superconductivity and Novel Magnetism **34**(1), 149 (2020).
[32] M. Lakshminadh, M. Murugan, G. S. V. R. K. Choudary, M. C. Varma, AIP Conference Proceedings **2269**, 030055 (2020).
[33] A. Mahesh Kumar, K. Srinivasa Rao, M. Chaitanya Varma, K. H. Rao, J.Magn. Magn. Mater, **471**, 262 (2019).
[34] R. Mondal, S. Dey, S. Majumder, A. Poddar, P. Dasgupta, S. Kumar, J. Magn. Magn. Mater. **448**, 135 (2018).
[35] Vladan Kusigerski, Erzsebet Illes, Jovan Blanusa, Saso Gyergyek, Marko Boskovic, Marija Perovic, Vojislav Spasojevic, J. Magn. Magn. Mater. **475**, 470 (2019).
[36] Ali Ghasemi, Ebrahim Ghasemi, Ebrahim Paimozd, J. Magn. Magn. Mater. **323**, 1541 (2011).
[37] Dongwook Lim, Hyungseok Kong, Chaewon Lim, Namil Kim, Sang Eun Shim, Sung-Hyeon Baeck, Int. J. Hydrogen Energ. **44**, 23775 (2019).
[38] Xian Ming Liu, Shao Yun Fu, Hong Mei Xial, Chuan Jun Huang, Physica B **370**, 14 (2005).
[39] M. A. Almessiere, A. V. Trukhanov, Y. Slimani, K. Y. You, S. V. Trukhanov, E. L. Trukhanova, F. Esa, A. Sadaqat, K. Chaudhary, M. Zdorovets, A. Baykal, Nanomaterials **9**, 202 (2019).
[40] S. T. Hussain, S. R. Gilani, S. D. Ali, H. S. Bhatti, Journal of alloys and compounds **544**, 99 2012).
[41] J. N. Pavan Kumar Chintala, S. Bharadwaj, M. Chaitanya Varma, G. S. V. R. K. Choudary, Journal of Physics and Chemistry of Solids **160**, 110298 (2022).
[42] P. Sivakumar, R. Ramesh, A. Ramanand, S. Ponnusamy, C. Muthamizhchelvan, Mater. Res. Bull. **46**, 2208 (2011)
[43] X. M. Liu, W. L. Gao, Mater. Manuf. Process. **27**, 905 (2012).
[44] J. Rodríguez-Carvajal, J. (2001). FullProf. CEA/Saclay, France.
[45] İsrafil Şabikoğlu, Levent Paralı, Ondrej Malina, Petr Novak, Josef Kaslik, Jiri Tucek, Jiri Pechousek, Jakub Navarik, Oldrich Schneeweiss, Progress in Natural Science: Materials

International **25**(3), 215 (2015).
[46] O. M. Hemeda, M. A. Amer, S. Aboul- Enein, M. A. Ahmed, physica status solidi (a) **156**(1), 29 (1996).
[47] R. D. Shannon, Acta crystallographica section A: crystal physics, diffraction, theoretical and general crystallography **32**(5), 751 (1976).
[48] R. T. Shannon, C. T. Prewitt, Acta Crystallographica Section B: Structural Crystallography and Crystal Chemistry **25**(5), 925 (1969).
[49] H. M. Zaki, H. A. Dawoud, Physica B **405**, 4476 (2010).
[50] N. A. Spaldin, New York, Cambridge University Press, 2011.
[51] S. Blundell, New York, Oxford University Press Inc, 2001.
[52] W. Sławinski, R. Przeniosło, I. Sosnowska, E. Suard, Condens.Matter **17**, 4605 (2005).
[53] T. R. K. Pydiraju, K. Srinivasa Rao, P. Appa Rao, M. Chaitanya Varma, A. Satish Kumar, K. H. Rao, Journal of Magnetism and Magnetic Materials **524**, 167662 (2021).
[54] S. Ayyappan, S. Philip Raja, C. Venkateswaran, John Philip, Baldev Raj, Appl. Phys. Lett. **96**, 143106 (2010).
[55] Zihan Wang, Qiao Yuan, Yunfei Zhang, Min Ma, Daojiang Gao, Jian Bi, Jiangtao Wu, Ceramics International **47**, 17877 (2021).